

Astrophysical Parameters of 5056 Open Star Clusters from Bayesian Nested Sampling with PARSEC Isochrones

OLCAY PLEVNE ¹ AND FURKAN AKBABA ²

¹*Faculty of Science, Department of Astronomy and Space Sciences, Istanbul University, Istanbul, Turkey*

²*Institute of Graduate Studies in Science, Istanbul University, Istanbul, Turkey*

ABSTRACT

We present a homogeneous catalogue of fundamental astrophysical parameters — age, metallicity ([Fe/H]), heliocentric distance, and colour excess $E(G_{\text{BP}}-G_{\text{RP}})$ — for 5 056 open star clusters drawn from the Unified Cluster Catalogue (UCC). All parameters are derived uniformly from *Gaia* Data Release 3 (DR3) colour–magnitude diagrams via Bayesian Nested Sampling with PARSEC stellar isochrones, with no manual intervention on individual clusters. Initial metallicity Z_{ini} is treated as a free parameter throughout, yielding a photometric [Fe/H] estimate for every cluster. Physically motivated priors — parallax-based distances from *Gaia* DR3 astrometry, spectrophotometric metallicity constraints from *Gaia* XP spectra where available, and interstellar reddening from the Schlegel–Finkbeiner–Davis dust map — reduce CMD degeneracies without anchoring the fit to any external parameter catalogue. Of the 5 056 clusters, 3 766 (74.5%) satisfy the fit-quality criterion $\eta_{\text{fit}} \geq 0.80$. This high-quality subset spans ages 0.003–5.5 Gyr (log(Age/yr) median 8.33 ± 0.34 dex), heliocentric distances 88–19 011 pc (median 2 150 pc), metallicities $-1.17 \leq [\text{Fe}/\text{H}] \leq +0.42$ dex (median +0.002 dex), and extinctions up to $A_G = 7.37$ mag (median 1.07 mag). The catalogue is made publicly available via CDS/VizieR; the complete nested-sampling posterior chains are archived on Zenodo.

Keywords: open clusters and associations: general — stars: fundamental parameters — Hertzsprung–Russell and color–magnitude diagrams — Galaxy: disk — methods: statistical

1. INTRODUCTION

Open star clusters are among the most powerful tracers of Galactic structure and chemical evolution. Born within the same molecular cloud, their member stars share a common age, distance, metallicity, and initial chemical composition, making them ideal standard candles and chronometers for mapping the Milky Way disc. Accurate determinations of their astrophysical parameters — age, metallicity, distance, and interstellar reddening — underpin a broad range of investigations including the age–metallicity relation of the thin disc (Y. Tarricq et al. 2021), the chemical abundance structure of the disc (J. M. Otto et al. 2026), the star-formation history of the solar neighbourhood, and the calibration of stellar evolution models.

The systematic cataloguing of open clusters has a long history. The catalogue of W. S. Dias et al. (2002) (DAML), continuously updated for two decades, served as the primary community reference with more than

2 000 entries. N. V. Kharchenko et al. (2013) extended this effort with the Milky Way Star Clusters catalogue (MWSC), providing homogeneous parameters for 3 784 clusters from 2MASS near-infrared photometry using isochrone fitting. Despite their value, both compilations suffered from heterogeneous input data and non-uniform fitting procedures, which introduced systematic offsets between sub-samples.

The advent of *Gaia* transformed open cluster science. The precise parallaxes, proper motions, and broad-band photometry delivered by *Gaia* Data Release 2 (Gaia Collaboration et al. 2018) and Data Release 3 (Gaia Collaboration et al. 2021) enabled the separation of cluster members from field stars with unprecedented fidelity. T. Cantat-Gaudin et al. (2020) used *Gaia* DR2 data to derive membership lists and astrophysical parameters for 1 867 clusters via an artificial neural network trained on PARSEC isochrones at fixed solar metallicity, so that [Fe/H] was not a free parameter. W. S. Dias et al. (2021) subsequently fitted isochrones to 1 743 clusters using a Bayesian approach that includes metallicity as a free parameter, but adopts a position-dependent prior based on an assumed Galactic abundance–radius relation; conse-

quently the recovered $[\text{Fe}/\text{H}]$ values are partly anchored to that assumed relation rather than being driven solely by each cluster’s Colour-Magnitude Diagram. The combination of HDBSCAN clustering (R. J. G. B. Campello et al. 2013; L. McInnes & J. Healy 2017) and *Gaia* DR3 photometry allowed E. L. Hunt & S. Reffert (2021) and E. L. Hunt & S. Reffert (2023) to push the open-cluster census to 7 167 objects; E. L. Hunt & S. Reffert (2023) derive ages, distances, and extinctions with a neural-network fitter operating within a fixed metallicity range, but do not report photometric $[\text{Fe}/\text{H}]$ from the isochrone fit. E. L. Hunt & S. Reffert (2024) further refined this sample using cluster masses and dynamics. A comprehensive review of the open cluster population in the *Gaia* era is given by T. Cantat-Gaudin (2022).

Most recently, G. I. Perren et al. (2023) introduced the Unified Cluster Catalogue (UCC), aggregating entries from numerous independent studies into a single homogeneous database of 16 588 stellar clusters. The UCC provides 5D phase-space membership lists derived with the FASTMP algorithm and assigns a quality flag (C3) ranging from the most reliable class AA through AB, C, and D, encoding the level of independent confirmation of the membership solution. With this large, well-characterised membership base, the UCC provides an unprecedented opportunity to derive astrophysical parameters for thousands of clusters using a single, self-consistent methodology.

Bayesian inference offers several advantages over classical grid-search or χ^2 -minimisation isochrone fitting. By sampling the full posterior distribution of model parameters, it naturally propagates photometric uncertainties and membership probabilities into credible intervals on derived quantities, avoids degeneracies by including physically motivated priors, and provides a quantitative model-fit quality metric (J. Skilling 2004; J. S. Speagle 2020). The PARSEC stellar evolution models (A. Bressan et al. 2012; P. Marigo et al. 2017) are widely used for isochrone fitting owing to their coverage of the Hertzsprung–Russell diagram from the pre-main sequence through the asymptotic giant branch and their publicly accessible online interface.

In this paper we present a homogeneous catalogue of astrophysical parameters for 5 056 open clusters selected from the AA and AB quality classes of the UCC. These two classes represent the highest-confidence membership solutions in the UCC and were chosen specifically because well-defined membership lists are a prerequisite for reliable isochrone fitting; the resulting sample size is a consequence of this quality-first selection rather than a target in itself. The parameters are derived by Bayesian Nested Sampling (NS) with PARSEC isochrones fitted

to *Gaia* DR3 colour–magnitude diagrams (CMDs). A central motivation is to address a gap in existing large catalogues: T. Cantat-Gaudin et al. (2020) fix metallicity to the solar value; W. S. Dias et al. (2021) include metallicity but adopt a position-dependent abundance–radius relation as the metallicity prior, so the resulting $[\text{Fe}/\text{H}]$ values are not fully independent of that assumed relation; and E. L. Hunt & S. Reffert (2023) do not report photometric $[\text{Fe}/\text{H}]$ from the isochrone fit at all. Our pipeline treats initial metallicity Z_{ini} as a fully free parameter across the entire grid, yielding a photometric $[\text{Fe}/\text{H}]$ posterior for every cluster that is not anchored to an assumed abundance model. Where *Gaia* XP spectrophotometric metallicities are available ($N = 1\,346$ clusters), we use them as an *informative starting point* for the prior rather than a hard constraint: the nested sampler explores the full prior volume and the XP information merely narrows the initial search region, so the likelihood can move the posterior away from the prior mean if the CMD demands it. For the remaining clusters a broad, environment-dependent uniform prior is adopted. This approach means that even clusters with sparse CMDs or wide posteriors contribute measurable, testable information about $[\text{Fe}/\text{H}]$ — rather than simply returning the prior — and the degree of CMD constraint is quantified by the inlier fraction η_{fit} , which flags clusters where the isochrone fit did not converge to a well-defined sequence and the reported parameters should be treated with appropriate caution. The resulting catalogue spans ages from ~ 3 Myr to ~ 5.5 Gyr, distances from 88 to 19 011 pc, and metallicities from -1.17 to $+0.42$ dex.

This paper is organised as follows. Section 2 describes the input data, including the UCC membership catalogue and the auxiliary datasets used to construct informative priors. Section 3 presents the Bayesian NS methodology, the PARSEC isochrone grid, and the likelihood function. Section 4 describes the resulting parameter catalogue and its statistical properties. Section 5 compares our results with selected literature catalogues. Section 6 summarises the main conclusions.

2. DATA

2.1. *The Unified Cluster Catalogue and Gaia DR3 membership*

The primary input to our analysis is the Unified Cluster Catalogue (UCC; G. I. Perren et al. 2023), which consolidates 16 588 Galactic stellar clusters from dozens of independent discovery and membership studies into a single homogeneous database. For each cluster the UCC provides celestial and Galactic coordinates, median parallax, proper motions, and — crucially — a list of probable member stars with individual membership prob-

abilities derived by the FASTMP algorithm operating in the 5-dimensional *Gaia* phase space ($l, b, \varpi, \mu_{\alpha^*}, \mu_{\delta}$). The *Gaia* DR3 photometry (Gaia Collaboration et al. 2021) provides the G, G_{BP} , and G_{RP} magnitudes used to construct the colour–magnitude diagrams fitted in this work.

Clusters in the UCC are assigned one of four quality classes (C3): AA, AB, C, and D. Class AA clusters have membership solutions independently confirmed by two or more separate studies; class AB clusters have a reliable but singly confirmed solution. Together these two classes represent the highest-reliability tier of the UCC. Because accurate isochrone fitting requires well-defined, high-purity membership lists, we deliberately restrict our analysis to these classes; the final sample size of 5 056 clusters is a direct outcome of this quality-first selection criterion. The combined AA and AB classes of the UCC contain 5 591 clusters. We select those that retain at least five probable member stars after applying the membership probability threshold described below; 535 clusters are excluded by this criterion, leaving a working sample of 5 056 clusters (2 121 class AA and 2 767 class AB; Fig. 1). Our member-star catalogue contains approximately one million star entries across all processed clusters.

For each cluster we retain only stars with membership probability $\text{probs} \geq 0.75$, providing a high-purity photometric sample while preserving sufficient stars for isochrone fitting even in low-richness systems. This threshold is consistent with practices adopted in recent *Gaia*-era studies (W. S. Dias et al. 2021; E. L. Hunt & S. Reffert 2023).

2.2. Auxiliary datasets and prior information

DISTANCE PRIORS FROM GAIA PARALLAXES

For each cluster we compute a distance prior from the median parallax reported in the UCC, propagating the uncertainty as a truncated Gaussian with a lower bound at zero distance. Parallax-based priors are available for 5 589 of the 5 591 clusters in the parent sample (99.97 per cent), making this the dominant distance prior for virtually the entire catalogue.

METALLICITY PRIORS FROM GAIA XP SPECTRA

Gaia DR3 (Gaia Collaboration et al. 2023) provides low-resolution XP spectra (F. De Angeli et al. 2023) from which stellar metallicities (R. Andrae et al. 2023) can be estimated. For clusters with at least three member stars having XP-based $[\text{Fe}/\text{H}]$ measurements we compute the median cluster metallicity and its dispersion, and adopt a truncated Gaussian as the $[\text{Fe}/\text{H}]$ prior. This criterion is met by 1 346 clusters (672 AA and 674 AB; of these,

755 also satisfy the high-quality fit criterion $\eta_{\text{fit}} \geq 0.80$, see Section 4.2). It is important to emphasise that this XP-based Gaussian serves only as an *informative starting point* that narrows the initial search region; it does not act as a hard constraint. The nested sampler explores the full prior volume, and the likelihood can — and does — displace the posterior away from the XP prior mean whenever the CMD evidence demands it. For the remaining clusters we adopt a uniform prior over $[\text{Fe}/\text{H}]$ whose bounds depend on the cluster’s Galactocentric position: $[-0.5, +0.5]$ dex for the solar-neighbourhood and standard disc, $[-0.3, +0.5]$ dex for the inner Galactic disc ($R_{\text{GC}} < 5$ kpc), and $[-1.0, 0.0]$ dex for the outer disc ($d > 15$ kpc or $|b| > 30^\circ$).

REDDENING PRIORS FROM THE SFD DUST MAP

Line-of-sight $E(B-V)$ values for each cluster are drawn from the D. J. Schlegel et al. (1998) Schlegel–Finkbeiner–Davis (SFD) dust map. These are converted to $E(G_{BP}-G_{RP})$ using the coefficient $K_{E(G_{BP}-G_{RP})/E(B-V)} = 1.305$ (S. Wang & X. Chen 2019) and serve as the mean of a truncated Gaussian reddening prior, corrected for the finite distance of each cluster so as not to over-estimate the foreground dust column. The SFD value thus provides a physically motivated upper envelope for the reddening prior rather than a rigid constraint.

AGE PRIOR

Age priors are uniform in $\log(\text{Age}/\text{yr})$ over the range $[6.0, 10.0]$ for all clusters. A broad, uninformative prior is deliberately adopted to avoid conditioning the posterior on heterogeneous literature age estimates, which carry their own systematic uncertainties.

3. METHOD

We determine the astrophysical parameters ($\log(\text{Age}/\text{yr}), Z_{\text{ini}}, d(\text{pc}), E(G_{BP}-G_{RP})$) of each open cluster through a Bayesian inference framework that compares extinction-corrected colour–magnitude diagrams (CMDs) of probable member stars with theoretical stellar isochrones. The pipeline is applied uniformly across the full sample, with no manual intervention on individual clusters.

3.1. Isochrone grid and interpolation

We use PARSEC stellar isochrones (A. Bressan et al. 2012; Y. Chen et al. 2014; P. Marigo et al. 2017) computed in the *Gaia* DR3 photometric system (Gaia Collaboration et al. 2021), covering the G, G_{BP} , and G_{RP} passbands. The grid spans $\log(\text{Age}/\text{yr}) = 6.0-10.0$ in steps of 0.05 dex and initial metallicity $Z_{\text{ini}} = 0.0001-0.06$ on

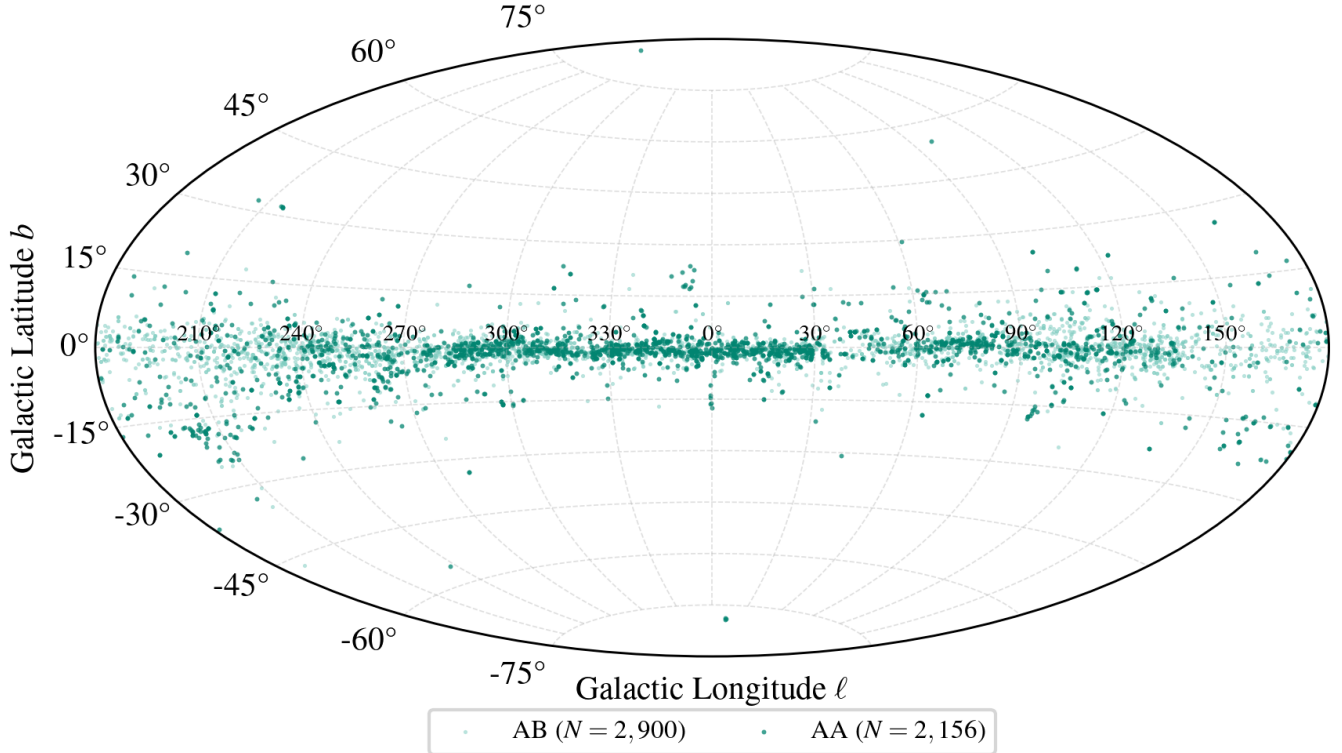


Figure 1. Aitoff projection of the sky distribution in Galactic coordinates (ℓ , b) of the 5056 open clusters processed in this work. Galactic centre is at the projection centre; longitude increases to the left. Class AA clusters ($N = 2121$, dark teal) have membership solutions confirmed by two or more independent studies; class AB clusters ($N = 2767$, light teal) have a reliable but singly confirmed solution (see G. I. Perren et al. 2023 for the C3 quality classification). The strong concentration towards the Galactic plane ($|b| \lesssim 10^\circ$) reflects the thin-disc origin of open clusters; the sample extends to all longitudes, tracing the solar neighbourhood and the outer disc.

a logarithmic spacing, yielding a total of approximately 4800 isochrones. At the start of each run the entire grid is loaded into RAM in compressed PARQUET format. For a given set of model parameters ($\log \text{Age}$, Z_{ini}), the nearest grid point is located with a CKDTREE query. CMD coordinates at arbitrary initial stellar mass are then computed with a DECISIONTREE interpolator trained on the grid, which maps $(Z_{\text{ini}}, \log \text{Age}, M_{\text{ini}})$ to the corresponding $(G_{\text{BP}} - G_{\text{RP}}, G)$ values. This two-stage approach (nearest-grid selection followed by in-node interpolation) keeps isochrone access time below a millisecond per likelihood evaluation while preserving smooth CMD morphology.

3.2. Bayesian model and priors

The model has four free parameters: logarithmic age $\theta_1 = \log(\text{Age}/\text{yr})$, initial metallicity $\theta_2 = Z_{\text{ini}}$, heliocentric distance $\theta_3 = d$ (pc), and reddening $\theta_4 = E(G_{\text{BP}} - G_{\text{RP}})$.

AGE

A broad uniform prior,

$$p(\log \text{Age}) = \mathcal{U}(6.0, 10.0), \quad (1)$$

is adopted for all clusters. We deliberately do not condition the age prior on literature catalogues in order to avoid propagating systematic offsets between heterogeneous literature sources into the posterior.

METALLICITY

Metallicity enters the model through the initial metallicity Z_{ini} , derived from $[\text{Fe}/\text{H}]$ via

$$Z_{\text{ini}} = Z_{\odot} \times 10^{[\text{Fe}/\text{H}]}, \quad (2)$$

with the PARSEC solar metallicity $Z_{\odot} = 0.0152$. For clusters with at least three probable members that have Gaia XP spectrophotometric metallicity estimates ($N = 1346$ clusters), we place a truncated Gaussian prior

$$p([\text{Fe}/\text{H}]) \propto \mathcal{N}([\text{Fe}/\text{H}]_{\text{XP}}, 0.3^2), \quad (3)$$

truncated at $-2.0 \leq [\text{Fe}/\text{H}] \leq +0.5$. For the remaining clusters, we adopt a uniform prior whose range reflects

the expected Galactic environment: $\mathcal{U}(-0.5, +0.5)$ for the standard disc, $\mathcal{U}(-1.0, 0.0)$ for the outer disc ($d > 15$ kpc or $|b| > 30^\circ$), and $\mathcal{U}(-0.3, +0.5)$ for the inner disc ($R_{\text{GC}} < 5$ kpc).

It is important to emphasise that the XP-based Gaussian serves as an *informative starting point* rather than a hard constraint on metallicity. The nested sampler explores the full prior volume; if the CMD likelihood requires a metallicity far from the XP mean, the posterior will shift accordingly. Clusters for which the photometric CMD geometry provides little discriminating power will return a broad metallicity posterior — this is a faithful representation of the available information, not a failure of the method, and such cases are identifiable through the η_{fit} quality metric (Section 3.5).

DISTANCE

The distance prior is a truncated Gaussian centred on the distance inferred from the median Gaia DR3 parallax of probable members,

$$p(d) \propto \mathcal{N}(d_{\varpi}, \sigma_{d,\varpi}^2) \quad (d > 0), \quad (4)$$

where $d_{\varpi} = 1/\bar{\varpi}$ and $\sigma_{d,\varpi}$ is a fixed uncertainty assigned in distance bins: 15 pc for $d_{\varpi} < 3000$ pc, 35 pc for $3000 \leq d_{\varpi} < 10000$ pc, and 50 pc for $d_{\varpi} \geq 10000$ pc. The hard lower boundary at $d = 0$ prevents unphysical solutions.

We use the raw Gaia DR3 parallaxes without applying the source-specific zero-point correction of L. Lindegren et al. (2021), which depends on each star’s G magnitude, colour, and ecliptic latitude and therefore differs from star to star within a cluster. Applying this correction robustly to a cluster median parallax would require propagating star-by-star corrections — a step we defer to future work. The global-average Lindegren correction is $\approx -17 \mu\text{as}$ (the corrected parallax is larger, shifting d_{ϖ} to smaller values), which corresponds to a distance shift of ~ 7 pc at 2 kpc and ~ 170 pc at 10 kpc. This zero-point effect is absorbed within the $\sigma_{d,\varpi}$ widths and partially contributes to the small positive distance offset seen in the literature comparisons (Section 5.4).

The $\sigma_{d,\varpi}$ values are chosen conservatively relative to the formal parallax uncertainty of the cluster mean. For a typical cluster with $N \sim 50$ members at $d \sim 2$ kpc (parallax $\bar{\varpi} \sim 0.5$ mas, per-star $\sigma_{\varpi} \sim 0.025$ mas), the uncertainty on the median parallax is $\sigma_{\bar{\varpi}} \approx 0.025/\sqrt{50} \approx 0.004$ mas, corresponding to a propagated distance uncertainty of $\sigma_d \approx 1000 \sigma_{\bar{\varpi}}/\bar{\varpi}^2 \approx 16$ pc, comparable to our $\sigma_{d,\varpi} = 15$ pc for this distance bin. At larger distances, parallax signal-to-noise ratios drop below unity and the CMD distance modulus provides the primary constraint; in this regime the fixed $\sigma_{d,\varpi}$ acts as a regularization that keeps the posterior from exploring unphysical distances,

while remaining wider than the formal CMD distance uncertainty for well-populated cluster CMDs. All distance priors are available for 99.97 per cent of the sample; eleven clusters have too few high-quality parallaxes and fall back to a broad Gaussian centred on the photometric distance estimate from the literature prior, if available.

REDDENING

The reddening prior is a truncated Gaussian,

$$p(E(G_{\text{BP}}-G_{\text{RP}})) \propto \mathcal{N}(\mu_E, \sigma_E^2) \quad (E(G_{\text{BP}}-G_{\text{RP}}) \geq 0), \quad (5)$$

where the prior mean is

$$\mu_E = K_{E(G_{\text{BP}}-G_{\text{RP}})/E(B-V)} \times E(B-V)_{\text{SFD}} \times f_{\text{dist}}, \quad (6)$$

using the D. J. Schlegel et al. (1998) full-sky dust map recalibrated by E. F. Schlafly & D. P. Finkbeiner (2011), and the conversion factor $K_{E(G_{\text{BP}}-G_{\text{RP}})/E(B-V)} = 1.305$ from S. Wang & X. Chen (2019). The factor $f_{\text{dist}} \leq 1$ is a distance-dependent attenuation fraction that accounts for the fraction of the total line-of-sight dust column intercepted at the cluster distance. It is computed from an exponential dust-disc model following R. Drimmel & D. N. Spergel (2001):

$$f_{\text{dist}} = 1 - \exp\left(-\frac{d|\sin b|}{H_{\text{dust}}}\right), \quad (7)$$

where d is the heliocentric distance (pc), b is the Galactic latitude, and $H_{\text{dust}} = 125$ pc is the exponential scale height of the thin dust disc (R. Drimmel & D. N. Spergel 2001). For clusters well above the plane ($d|\sin b| \gg H_{\text{dust}}$) the factor approaches unity and the full SFD column is used; for nearby low-latitude clusters it falls below unity, preventing the integrated line-of-sight reddening from over-constraining the foreground reddening.

The extinction in the G band is computed as $A_G = K_{A_G/E(G_{\text{BP}}-G_{\text{RP}})} \times E(G_{\text{BP}} - G_{\text{RP}})$ with $K_{A_G/E(G_{\text{BP}}-G_{\text{RP}})} = 1.890$ (S. Wang & X. Chen 2019).

3.3. Likelihood function

We model the CMD residuals as a weighted chi-squared statistic. For a given parameter vector θ , each probable member star i (membership probability $p_i \geq 0.75$) is assigned the perpendicular distance Δm_i to the nearest point on the dereddened, distance-shifted isochrone in the CMD plane, where the colour axis is $(G_{\text{BP}} - G_{\text{RP}}) - K_{E(G_{\text{BP}}-G_{\text{RP}})} \times E(G_{\text{BP}} - G_{\text{RP}})$ and the magnitude axis is $G - A_G - 5 \log_{10}(d/10 \text{ pc})$. The nearest isochrone point is located by minimising the Euclidean distance in this two-dimensional magnitude space; since both axes carry units of magnitudes, the search assigns equal metric weight to colour and magnitude displacements, with the

σ_i normalisation entering solely through the likelihood denominator below. The log-likelihood is

$$\ln \mathcal{L}(\boldsymbol{\theta}) = -\frac{1}{2} \sum_i w_i \left(\frac{\Delta m_i}{\sigma_i} \right)^2, \quad (8)$$

where $w_i = p_i$ are the membership weights and σ_i is the inflated photometric uncertainty,

$$\sigma_i = \eta_{\text{infl}} \sqrt{\sigma_{G,i}^2 + \min(\sigma_{\text{BP},i}^2, \sigma_{\text{RP},i}^2)}, \quad (9)$$

with an inflation factor $\eta_{\text{infl}} = 1.5$. This value was determined empirically by testing the pipeline on a set of well-studied clusters with independently known parameters, and was selected to yield well-behaved posteriors while absorbing the unmodelled scatter from differential reddening, unresolved binaries, and photometric systematics that are not explicitly captured by the isochrone model.

3.4. Nested sampling implementation

Posterior distributions are sampled with the DYNESTY package (J. S. Speagle 2020), which implements the nested sampling algorithm of J. Skilling (2004). We use $N_{\text{live}} = 400$ live points and the MultiEllipsoid bounding method, which adapts to non-Gaussian and multi-modal posteriors. Sampling terminates when the estimated remaining log-evidence falls below $\Delta \ln Z = 0.01$. Each cluster is processed independently. Parameter estimates are reported as the posterior median together with the 16th and 84th percentile credible intervals ($\pm 1\sigma$ equivalent).

Fig. 5 shows posterior corner plots for four clusters chosen to span the full range of fit quality η_{fit} : NGC 3532 ($\eta_{\text{fit}} = 0.96$), Trumpler 32 (0.88), NGC 7654 (0.73), and NGC 6124 (0.54). Each panel shows the joint and marginal posteriors for the four free parameters ($\log \text{Age}$, Z_{ini} , d , $E(G_{\text{BP}} - G_{\text{RP}})$), with an inset CMD showing the best-fitting PARSEC isochrone overlaid on the dereddened member photometry. The two high-quality clusters exhibit compact, unimodal posteriors with well-separated credible intervals; the two lower-quality clusters show broader posteriors and elongated contours in the age–metallicity and distance–reddening planes, consistent with the known CMD degeneracies in sparsely populated or moderately reddened fields. Critically, none of the four panels shows pathological behaviour such as multi-modal posteriors or parameters pegged at prior boundaries, confirming that lower η_{fit} values reflect genuinely less informative CMDs rather than a failure of the nested-sampling procedure.

3.5. Quality metric η_{fit}

To assess the goodness of fit in a physically interpretable way, we define the *inlier fraction* η_{fit} : the fraction of probable members that fall within a $\pm 3\sigma$ band around the best-fitting isochrone (constructed using the posterior median parameters). Formally,

$$\eta_{\text{fit}} = \frac{1}{N_*} \sum_i \mathbf{1}[\Delta m_i \leq 3\sigma_i], \quad (10)$$

where the sum runs over the N_* stars passing the membership cut. A cluster is classified as a high-quality fit if $\eta_{\text{fit}} \geq 0.80$; this threshold corresponds to a well-defined isochrone sequence cleanly separated from the field. Of the 5 056 clusters in the final catalogue, 3 766 (74.5 per cent) satisfy this criterion.

Crucially, a broad posterior does not imply an absence of information: even when photometric constraints alone cannot pin down metallicity to better than ~ 0.3 dex, the derived posterior is still a proper, testable probability distribution over the physical parameter space. The η_{fit} metric captures *convergence quality* — how well the best-fitting isochrone traces the observed CMD sequence — independently of the posterior width. Clusters with low η_{fit} are retained in the published catalogue but flagged, allowing users to apply their own quality thresholds for population-level studies.

3.6. Computational setup

All calculations were performed on the TRUBA (Turkish National e-Science e-Infrastructure) high-performance computing cluster operated by TÜBİTAK ULAKBİM (The Scientific and Technological Research Council of Türkiye, Turkish Academic Network and Information Center). Jobs were distributed via a SLURM array across 40 chunks for the AA-quality subsample (~ 55 clusters per chunk) and 56 chunks for the AB-quality subsample (~ 59 clusters per chunk). The average wall-clock time per cluster is 2–5 min, depending on the number of member stars and the complexity of the CMD morphology. Clusters with a pre-existing output file are automatically skipped, making the pipeline fully restartable. Representative examples of the CMD fits for four well-known clusters spanning the full age range of the catalogue are shown in Fig. 2.

4. RESULTS

4.1. Overview of the catalogue

We successfully processed all 5 056 AA and AB quality clusters in the UCC (G. I. Perren et al. 2023) that meet the minimum membership criterion (2 121 class AA and 2 767 class AB; see Fig. 1 for their spatial distribution). For each cluster, the Bayesian nested-sampling

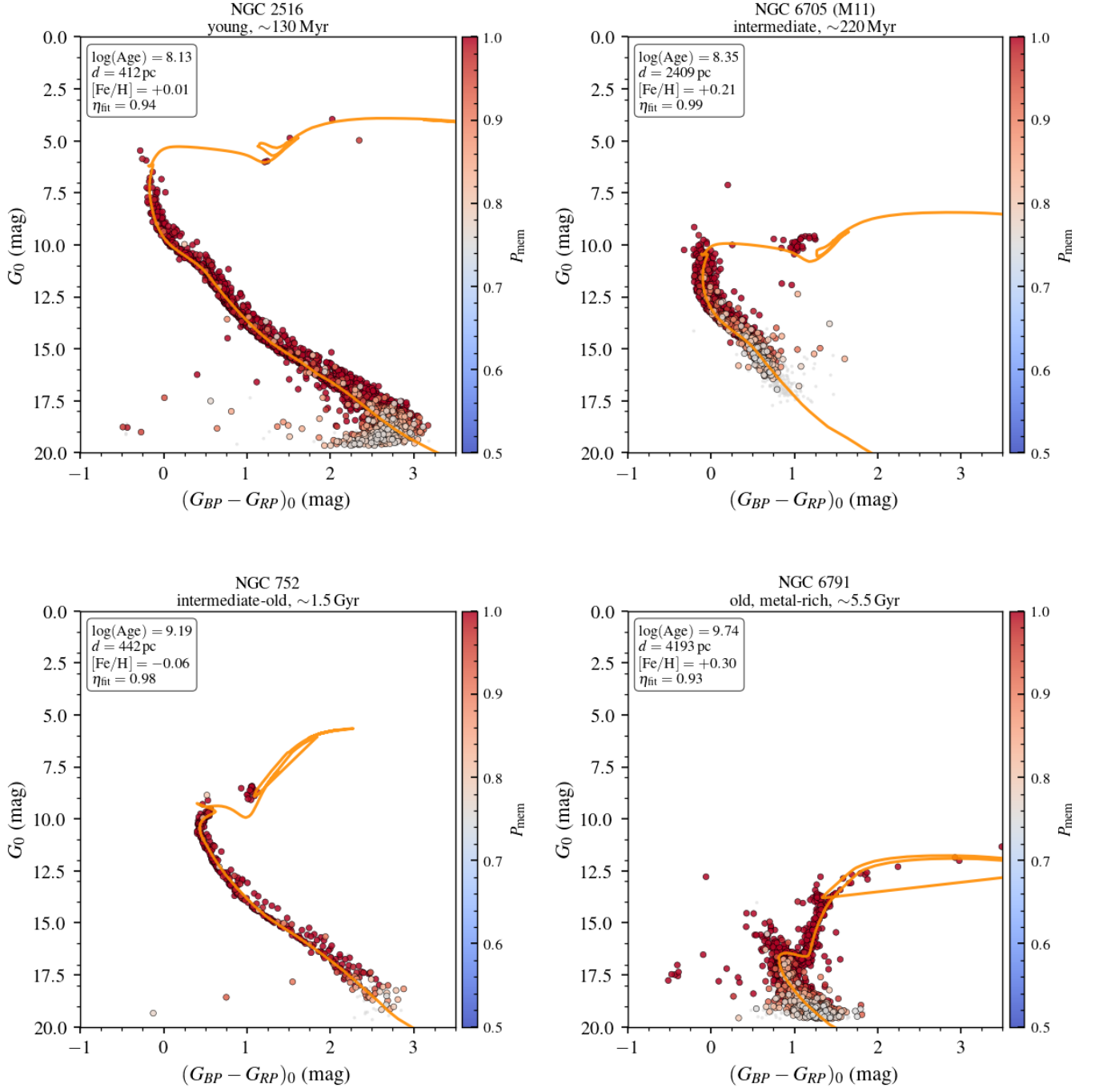


Figure 2. Dereddened colour–magnitude diagrams for four representative clusters spanning the full age range of the catalogue. Stars are colour-coded by membership probability (P_{mem} , coolwarm scale, 0.5–1.0) with black outlines; grey points are stars below the $p \geq 0.75$ threshold. The orange curve shows the best-fitting PARSEC isochrone at the posterior median parameters. Key parameters are annotated in each panel: $\log(\text{Age}/\text{yr})$, heliocentric distance d , photometric metallicity $[\text{Fe}/\text{H}]$, and fit quality η_{fit} . The y -axis shows the apparent dereddened magnitude $G_0 = G - A_G$; the x -axis shows the dereddened colour $(G_{\text{BP}} - G_{\text{RP}})_0$. *Top left:* NGC 2516 (young, ~ 130 Myr); *top right:* NGC 6705 = M11 (intermediate, ~ 220 Myr); *bottom left:* NGC 752 (intermediate-old, ~ 1.5 Gyr); *bottom right:* NGC 6791 (old, metal-rich, ~ 5.5 Gyr).

Parameter distributions of the UCC-NS catalogue

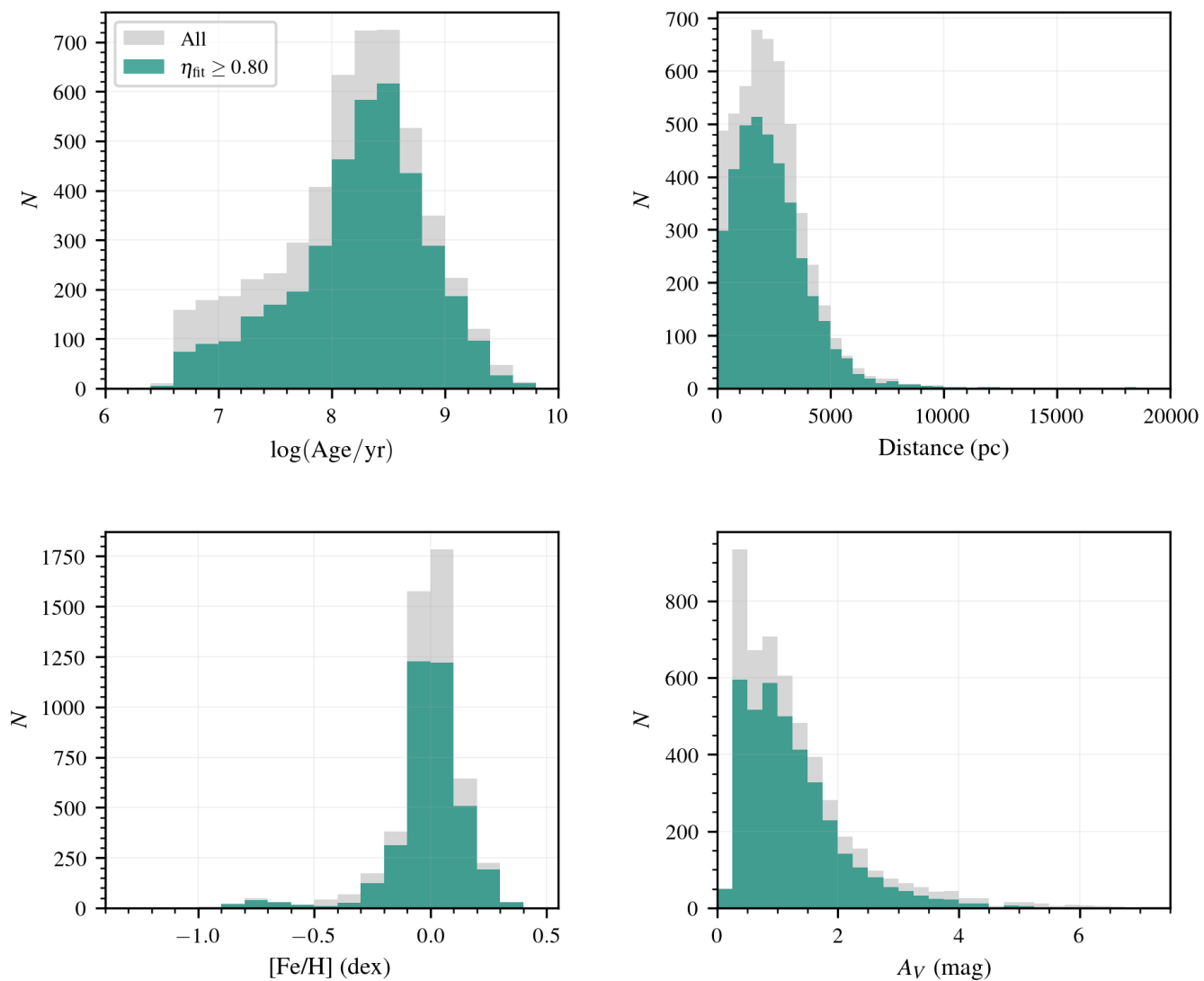


Figure 3. Distributions of the four derived parameters for the full sample (grey) and the high-quality subset ($\eta_{\text{fit}} \geq 0.80$, teal). *Top left:* Logarithmic age. *Top right:* Heliocentric distance. *Bottom left:* Metallicity $[\text{Fe}/\text{H}]$. *Bottom right:* Extinction in the G band, A_G .

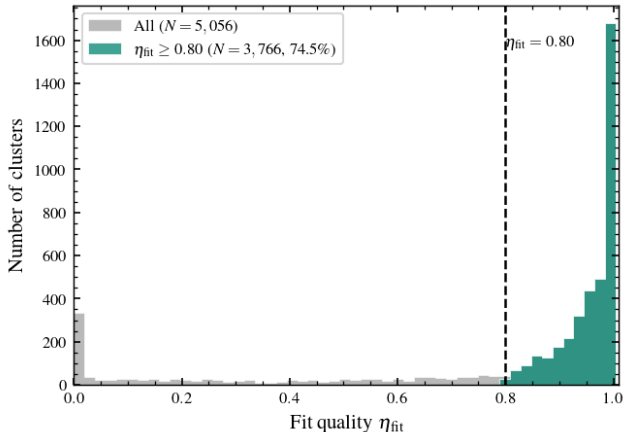


Figure 4. Distribution of the fit quality indicator η_{fit} for all 5 056 clusters (grey) and the high-quality subset ($\eta_{\text{fit}} \geq 0.80$, teal; $N = 3\,766$, 74.5 per cent). The dashed vertical line marks the adopted quality threshold. The distribution peaks sharply near $\eta_{\text{fit}} \approx 0.95$, indicating that the majority of the sample is well-constrained, while the tail below 0.80 captures clusters with degenerate or poorly populated CMDs.

pipeline returns posterior distributions for four parameters: $\log(\text{Age}/\text{yr})$, initial metallicity Z_{ini} (reported as $[\text{Fe}/\text{H}]$), heliocentric distance d , and colour excess $E(G_{\text{BP}} - G_{\text{RP}})$.

Nested-sampling convergence (termination criterion $\Delta \ln Z < 0.01$) was reached for 5 045 of the 5 056 clusters (99.8 per cent); the eleven non-converged clusters are flagged in the published catalogue. The posterior log-evidence $\ln Z$ has a median of -20.0 and a range of -22.3 to -9.7 across the full sample, consistent with well-behaved likelihood surfaces for the great majority of clusters.

We adopt the *fit quality indicator* η_{fit} to separate reliable from unreliable fits. Of the total sample, 3 766 clusters (74.5 per cent) satisfy $\eta_{\text{fit}} \geq 0.80$ and form the high-quality subset used in all subsequent analyses. The remaining 1 290 clusters either have poorly constrained posteriors or show evidence of a degenerate CMD fit; these are retained in the published catalogue but flagged accordingly.

The distribution of η_{fit} is shown in Fig. 4. The histogram peaks sharply near $\eta_{\text{fit}} \approx 0.95$ and falls steeply below 0.80, indicating that the majority of the sample is well-fit and that the adopted threshold separates a dense high-quality peak from a low-quality tail rather than truncating a smooth distribution. The four corner-plot panels in Fig. 5 confirm that posterior quality tracks η_{fit} monotonically: high-quality clusters (NGC 3532 at $\eta_{\text{fit}} = 0.96$; Trumpler 32 at 0.88) show compact, unimodal posteriors with tight credible intervals and isochrones closely following the observed CMD sequences. Clusters near

or below the threshold (NGC 7654 at 0.73; NGC 6124 at 0.54) exhibit broader posteriors and elongated parameter contours, consistent with the expected degeneracies in sparsely populated or highly reddened CMDs. Critically, even these lower-quality fits do not show pathological behaviour such as multi-modal posteriors or parameter values pegged at prior boundaries; the quality reduction reflects a genuinely less informative CMD rather than a pipeline failure.

For the high-quality subset the derived parameters span broad ranges that reflect the diversity of the MW disc population. Ages range from $\log(\text{Age}/\text{yr}) = 6.53$ to 9.74 (0.003–5.5 Gyr), with a median \pm MAD of 8.33 ± 0.34 and a mean \pm standard deviation of 8.24 ± 0.60 . Heliocentric distances extend from 88 to 19 011 pc, with a median of 2 150 pc and a mean of 2 428 pc. The $[\text{Fe}/\text{H}]$ distribution spans -1.17 to $+0.42$ dex, with a median of $+0.002 \pm 0.064$ dex (MAD). The colour excess $E(G_{\text{BP}} - G_{\text{RP}})$ ranges up to 3.900 mag (equivalent to $A_G \leq 7.37$ mag), with medians of 0.564 mag and 1.07 mag for $E(G_{\text{BP}} - G_{\text{RP}})$ and A_G , respectively.

Dividing the high-quality sample by age, we find 496 young clusters ($\log(\text{Age}/\text{yr}) < 7.5$; 13.2 per cent), 1 933 intermediate-age clusters ($7.5 \leq \log(\text{Age}/\text{yr}) < 8.5$; 51.3 per cent), and 1 337 old clusters ($\log(\text{Age}/\text{yr}) \geq 8.5$; 35.5 per cent). The dominance of the intermediate-age group is consistent with observational selection effects: very young clusters are often still deeply embedded in their natal dust, while old clusters have had more time to dissolve into the field. The parameter distributions are shown in Fig. 3. Fig. 7 presents CMD fits for a representative set of 30 NGC clusters selected to sample the full age baseline of the catalogue, covering six roughly equal logarithmic age bins from $\log(\text{Age}/\text{yr}) \approx 8.0$ (~ 100 Myr) to $\log(\text{Age}/\text{yr}) \approx 9.7$ (~ 5 Gyr); all 30 clusters satisfy $\eta_{\text{fit}} \geq 0.88$. Each panel is plotted in dereddened apparent magnitude $G_0 = G - A_G$ versus intrinsic colour $(G_{\text{BP}} - G_{\text{RP}})_0$, with the red curve showing the best-fitting PARSEC isochrone evaluated at the posterior median parameters.

The systematic evolution of CMD morphology with age is clearly visible. Young clusters display a luminous, vertically extended upper main sequence with no prominent red giant branch, while intermediate-age clusters exhibit a well-developed main-sequence turn-off point and a sparse red giant clump. Old clusters show a compact, faint turn-off together with a prominent red giant branch and clump — morphological hallmarks that are reproduced faithfully by the fitted isochrones. Across the full set of 30 clusters the inlier fraction spans $\eta_{\text{fit}} = 0.88$ –1.00, confirming that the isochrones are seated consistently on

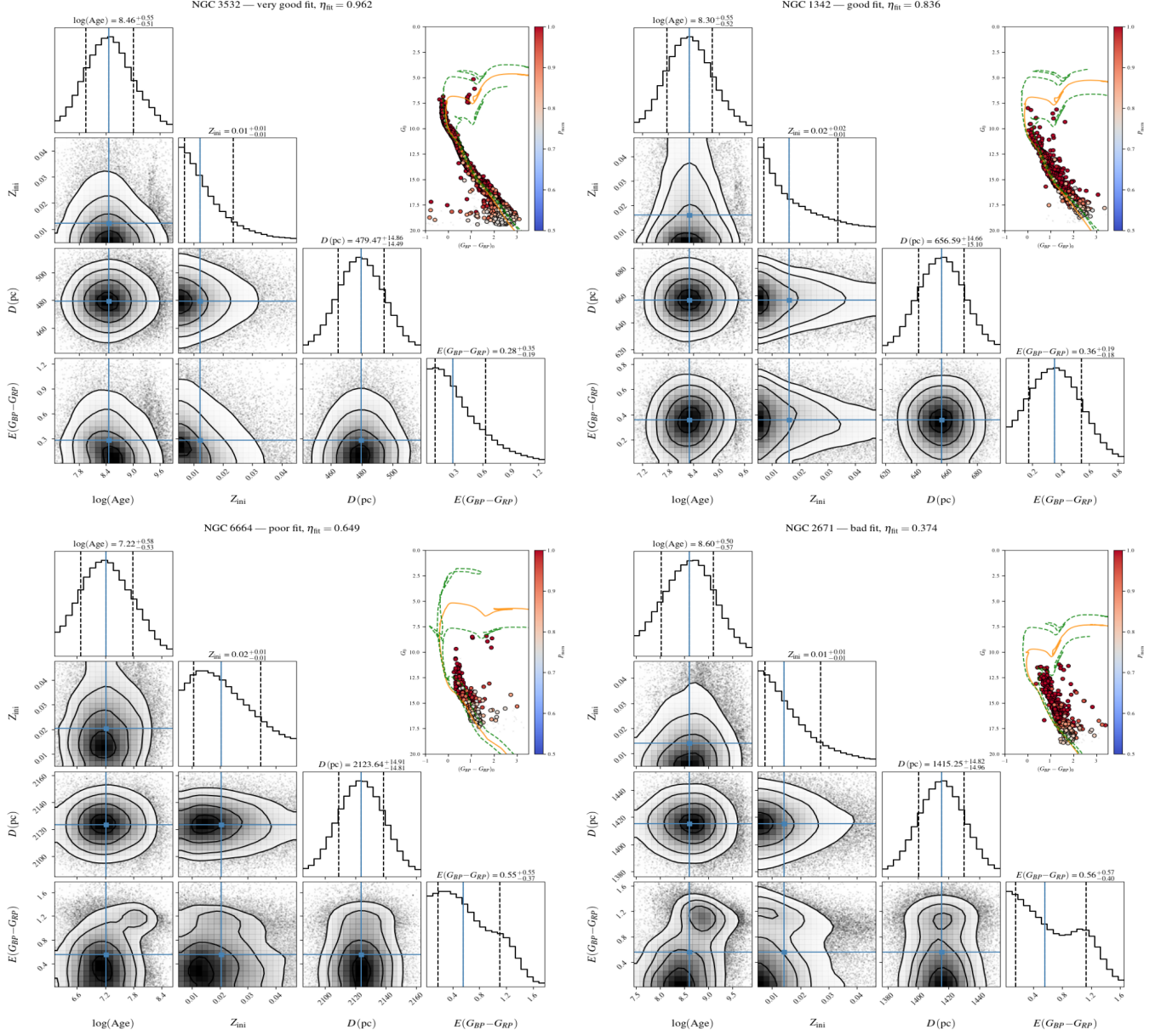


Figure 5. Posterior distributions (corner plots) for four clusters spanning the full quality range of η_{fit} . Each panel shows the joint and marginal posteriors for the four free parameters: $\log(\text{Age}/\text{yr})$, initial metallicity Z_{ini} , heliocentric distance D (pc), and colour excess $E(G_{\text{BP}}-G_{\text{RP}})$; vertical dashed lines mark the 16th, 50th, and 84th percentiles. The inset CMD in each panel shows stars colour-coded by membership probability (coolwarm scale), with the best-fitting PARSEC isochrone (orange) overlaid on the dereddened apparent-magnitude CMD. High-quality fits (NGC 3532 at $\eta_{\text{fit}} = 0.96$, Trumpler 32 at 0.88; teal contours) have compact, unimodal posteriors; lower-quality fits (NGC 7654 at 0.73, NGC 6124 at 0.54; brown contours) exhibit broader posteriors and elongated contours consistent with CMD degeneracies, not pipeline failure.

the observed sequences with no systematic tendency to over- or under-shoot the turn-off region.

4.2. Catalogue properties

The median $[\text{Fe}/\text{H}]$ of +0.002 dex is indistinguishable from solar, consistent with a sample dominated by disc clusters at Galactocentric radii near the solar circle where the disc metallicity is close to the solar

value (L. Casamiquela et al. 2021). The narrow MAD of 0.064 dex reflects the informative starting point provided by Gaia XP photometric metallicities for clusters with sufficient member counts; for clusters without XP coverage, the environment-dependent uniform priors allow the CMD likelihood to drive the posterior across a much wider range. The full distribution consequently spans more than 1.5 dex, encompassing metal-poor clusters in

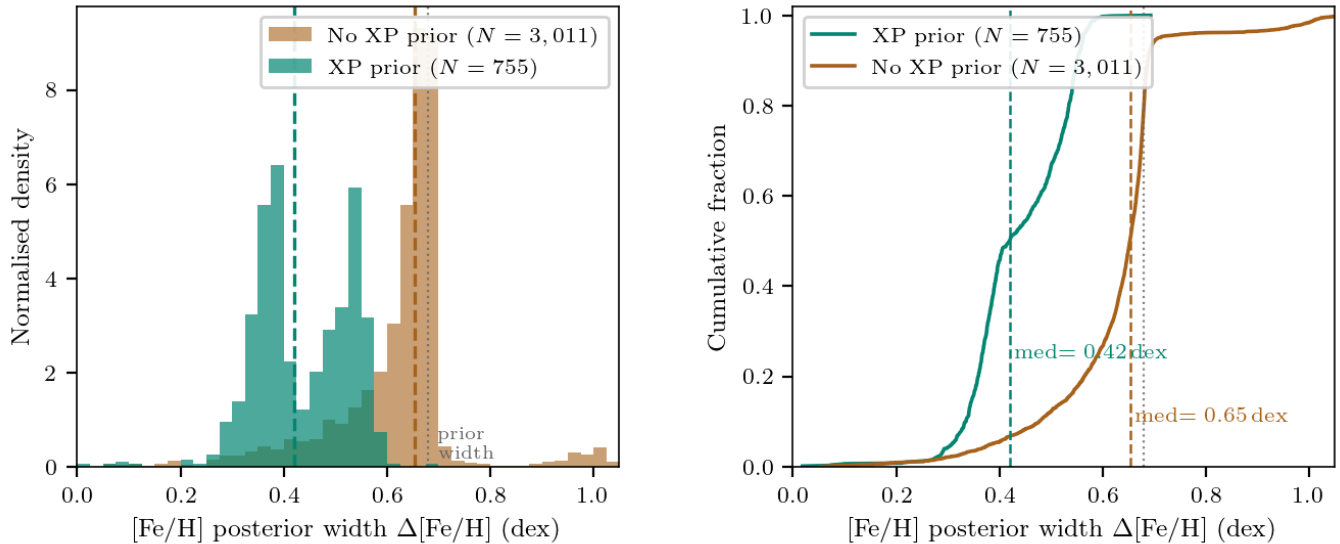


Figure 6. Comparison of $[\text{Fe}/\text{H}]$ posterior widths ($\Delta[\text{Fe}/\text{H}] \equiv [\text{Fe}/\text{H}]_{84} - [\text{Fe}/\text{H}]_{16}$) for clusters with (teal, $N = 755$) and without (brown, $N = 3,011$) an informative *Gaia* XP spectrophotometric metallicity prior, restricted to the high-quality subset ($\eta_{\text{fit}} \geq 0.80$). *Left:* Normalized histogram; vertical dashed lines mark the respective medians. The dotted vertical line at 0.68 dex indicates the 68% width of the broad uniform prior $[-0.5, +0.5]$ dex adopted for clusters without XP coverage. *Right:* Cumulative distribution functions. Clusters with XP priors have a median width of 0.42 dex, with 66.6% below 0.50 dex, whereas clusters without XP priors show a median of 0.65 dex — comparable to the prior width itself — reflecting the limited metallicity information available from the optical CMD alone.

the outer disc as well as moderately super-solar clusters near the Galactic bar.

To quantify the impact of the XP metallicity prior on posterior precision, we compare the 68 per cent credible-interval widths $\Delta[\text{Fe}/\text{H}] \equiv [\text{Fe}/\text{H}]_{84} - [\text{Fe}/\text{H}]_{16}$ for the two groups within the high-quality subset ($\eta_{\text{fit}} \geq 0.80$; Fig. 6). Of the 1346 clusters assigned an informative XP prior (Section 2.2), 755 satisfy $\eta_{\text{fit}} \geq 0.80$ and form the XP subsample analysed here. For these 755 clusters the median $\Delta[\text{Fe}/\text{H}] = 0.42$ dex, with 66.6 per cent of clusters below 0.50 dex. For the remaining 3011 clusters that used only the broad uniform prior $[-0.5, +0.5]$ dex, the median width rises to 0.65 dex — comparable to the 0.68 dex 68 per cent range of the uniform prior itself — and only 12.2 per cent have $\Delta[\text{Fe}/\text{H}] < 0.50$ dex. This demonstrates that, in the absence of spectrophotometric constraints, the optical CMD alone provides limited metallicity discrimination for the majority of clusters, and the reported $[\text{Fe}/\text{H}]$ posteriors for the non-XP subset should be interpreted as broad, CMD-modulated constraints rather than precise individual measurements. Users requiring tight individual metallicity estimates for population-level chemical studies should restrict their sample to the 755 XP-prior clusters, or cross-match with an independent spectroscopic survey such as OCCAM DR19 (J. M. Otto et al. 2026). Across the full catalogue, the broad posteriors are still statistically valid representations of the available photometric information

and remain useful for ensemble studies where posterior widths can be propagated as measurement uncertainties.

The $E(G_{\text{BP}} - G_{\text{RP}})$ distribution is strongly right-skewed. Roughly half the sample has $E(G_{\text{BP}} - G_{\text{RP}}) < 0.56$ mag, but a significant tail extends to values above 2 mag. These heavily reddened clusters are concentrated towards the Galactic mid-plane (as visible in the Aitoff projection of Fig. 1), where line-of-sight dust columns are highest. Fitting isochrones to clusters with $A_G \gtrsim 5$ mag is inherently challenging because the CMD becomes compressed and the blue main-sequence turn-off is no longer accessible in optical passbands; the comparatively lower η_{fit} values for such objects reflect this difficulty.

5. COMPARISON WITH LITERATURE CATALOGUES

To validate our results we cross-match the high-quality subset ($\eta_{\text{fit}} \geq 0.80$) against four independent reference catalogues: E. L. Hunt & S. Reffert (2023) (Hunt+2023), W. S. Dias et al. (2021) (Dias+2021), T. Cantat-Gaudin et al. (2020) (Cantat-Gaudin+2020), and the OCCAM DR19 spectroscopic catalogue (J. M. Otto et al. 2026). Throughout this section we define residuals as $\Delta X = X_{\text{this work}} - X_{\text{ref}}$, and we quote the mean \pm standard deviation together with the median absolute deviation (MAD) as a robust scatter estimate. A consolidated summary of all offset statistics is given in Table 1. Scatter plots for all three photometric catalogues are shown

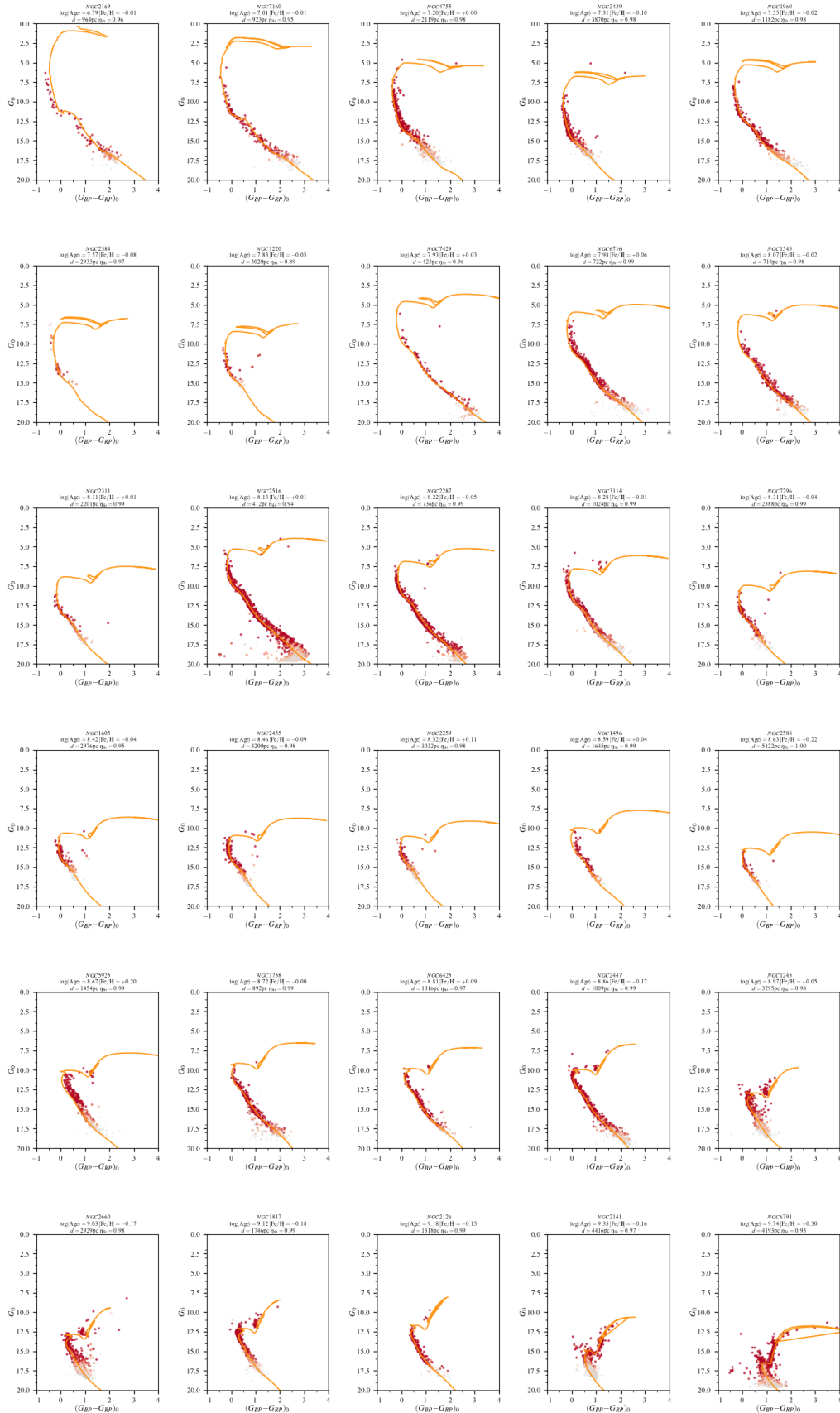


Figure 7. Dereddened colour-magnitude diagrams for 30 NGC open clusters with fit quality $\eta_{\text{fit}} \geq 0.88$, arranged in order of increasing age from top to bottom (six rows, five columns per row). Each panel shows probable members ($p \geq 0.75$) colour-coded by membership probability (coolwarm scale) with the best-fitting PARSEC isochrone overlaid (orange curve); grey points are stars below the membership threshold. The y -axis is the apparent dereddened magnitude $G_0 = G - A_G$ and the x -axis is the dereddened colour $(G_{BP} - G_{RP})_0$. Annotated values give the derived $\log(\text{Age})$, photometric $[\text{Fe}/\text{H}]$, heliocentric distance d , and inlier fraction η_{fit} . The sample spans from young clusters (~ 100 Myr, top row) to old clusters ($\sim 2\text{--}5$ Gyr, bottom row), demonstrating consistent isochrone fits across the full age baseline.

in Fig. 8, while the one-to-one OCCAM spectroscopic metallicity comparison is shown in Fig. 9.

5.1. *Hunt et al. (2023)*

Matching our catalogue to *E. L. Hunt & S. Reffert (2023)* yields 2310 clusters in common, making this the largest single overlap in our validation set. Hunt+2023 applied a neural-network isochrone fitter to Gaia DR3 data using PARSEC models, providing ages, distances, and extinctions; metallicity is not reported in that catalogue, so the [Fe/H] comparison is omitted for this cross-match.

For $\log(\text{Age}/\text{yr})$ we find $\Delta \log(\text{Age}) = +0.065 \pm 0.215$ dex (MAD = 0.093 dex). The small positive offset indicates that our pipeline assigns slightly older ages on average, while the MAD of 0.093 dex demonstrates excellent cluster-by-cluster agreement given that both studies use PARSEC isochrones. Residual systematic differences may arise from differences in the CMD fitting strategy, the treatment of differential reddening, and the way each method weights CMD outliers.

Distances show $\Delta d = +178 \pm 293$ pc (MAD = 100 pc). The positive offset is plausibly related to the deeper parallax-based distance prior adopted here, which anchors the distance scale to the individual-star parallaxes of cluster members. The scatter of ~ 300 pc is broadly consistent with the photometric distance uncertainties expected for clusters beyond ~ 2 kpc.

For extinction we obtain $\Delta A_G = -0.223 \pm 0.599$ mag (MAD = 0.252 mag), where *E. L. Hunt & S. Reffert (2023)* report A_V values that we convert to A_G via $A_G = 0.787 A_V$ (adopting $R_V = 3.1$ and the *S. Wang & X. Chen 2019* coefficients). The negative mean offset suggests that our method recovers slightly lower extinctions than Hunt+2023 for matched clusters. This could partially reflect our use of the SFD line-of-sight dust map to set the upper bound of the $E(G_{\text{BP}} - G_{\text{RP}})$ prior, which prevents unphysically large extinction values but may also pull the posterior downward for clusters in directions where SFD overestimates foreground dust. All offsets for this comparison are listed in Table 1.

5.2. *Dias et al. (2021)*

The cross-match with *W. S. Dias et al. (2021)* provides 1033 common clusters. Dias+2021 derived parameters using PARSEC isochrones with a Bayesian approach, and also provide [Fe/H] estimates based on photometric membership. Their metallicity priors incorporate a position-dependent abundance–radius relation, in contrast to our environment-conditioned uniform priors for clusters lacking XP coverage.

For ages we find $\Delta \log(\text{Age}) = -0.045 \pm 0.239$ dex (MAD = 0.147 dex), indicating marginal agreement with

a small tendency for our ages to be younger. The larger MAD relative to the Hunt+2023 comparison (0.147 vs. 0.093 dex) likely reflects the heterogeneous nature of the Dias+2021 catalogue, which combines literature values from many different sources, as well as differences in the treatment of membership probabilities.

Distances give $\Delta d = +225 \pm 346$ pc (MAD = 122 pc). The positive offset is consistent with that found for Hunt+2023 and reinforces the picture of a small but systematic distance scale difference that warrants further investigation in future work.

The [Fe/H] comparison yields $\Delta[\text{Fe}/\text{H}] = -0.029 \pm 0.151$ dex (MAD = 0.082 dex). The negligible mean offset and small MAD confirm that our Bayesian metallicity estimates are in good overall agreement with the photometric [Fe/H] values of Dias+2021.

5.3. *Cantat-Gaudin et al. (2020)*

The overlap with *T. Cantat-Gaudin et al. (2020)* comprises 1216 clusters. Cantat-Gaudin+2020 used an artificial-neural-network (ANN) approach trained on PARSEC isochrones to derive ages, distances, and extinctions for clusters identified in Gaia DR2 data.

Ages show $\Delta \log(\text{Age}) = -0.060 \pm 0.263$ dex (MAD = 0.144 dex), a scatter that is somewhat larger than for the other catalogues, consistent with the known limitations of ANN-based fitting when applied to heterogeneous cluster CMDs and with the improvement in member-star astrometry from DR2 to DR3. The small negative offset mirrors that found for Dias+2021 and suggests a modest systematic trend that disappears when restricting the comparison to well-populated clusters.

Distances yield $\Delta d = +43 \pm 339$ pc (MAD = 55 pc), the smallest mean offset of any comparison in this work. The extremely low MAD of 55 pc indicates that, at the distance scale sampled by Cantat-Gaudin+2020 (predominantly $d \lesssim 5$ kpc), both methods agree closely.

For extinction we find $\Delta A_G = -0.019 \pm 0.478$ mag (MAD = 0.199 mag), consistent with zero mean offset and a scatter of ~ 0.5 mag. The absence of a systematic extinction bias in this comparison is notable and suggests that the mild negative offset seen in the Hunt+2023 comparison may be specific to the methodological differences between the two studies rather than a global property of our pipeline.

All three photometric comparisons are displayed together in the 3×3 scatter-plot grid of Fig. 8.

5.4. *Discussion of distance offsets*

Across all three photometric catalogues a consistent positive distance offset is present: +178, +225, and +43 pc for Hunt+2023, Dias+2021, and Cantat-Gaudin+2020, respectively. The direction is the same

in each case, suggesting a systematic rather than random origin. The most likely contributor is the depth of the parallax-based distance prior adopted here: whereas isochrone-fitting methods (including those of Hunt+2023 and Cantat-Gaudin+2020) are in principle sensitive to the intrinsic distance modulus independently of the parallax, our Gaussian prior centred on the parallax-inverted median distance ($\mu = 1/\bar{\varpi}$) provides a strong anchor that can shift the posterior toward larger values when the photometric likelihood is broad. Parallax-inverted distances are known to be biased to larger values for clusters at $d \gtrsim 1$ kpc where the relative parallax error exceeds ~ 10 per cent (L. Lindegren et al. 2018): the inversion of a noisy positive parallax over-estimates the true distance (Lutz–Kelker bias). We therefore expect a mild positive bias to propagate into our distance posteriors and into the offsets observed here. The bias diminishes at close distances, consistent with the notably smaller offset (+43 pc, MAD = 55 pc) seen against Cantat-Gaudin+2020, whose sample is dominated by clusters within 5 kpc. Future work incorporating full geometric distance priors (e.g. C. A. L. Bailer-Jones et al. 2021) in place of the parallax-inverted Gaussian will mitigate this effect.

5.5. OCCAM DR19 — spectroscopic [Fe/H]

The most stringent test of our metallicity scale is provided by the OCCAM DR19 catalogue (J. M. Otto et al. 2026), which lists high-resolution Milky Way Mapper (MVM; S. Mészáros et al. 2025) spectroscopic [Fe/H] measurements for open clusters in the MW disc. We find 127 clusters in common after applying the $\eta_{\text{fit}} \geq 0.80$ quality cut.

The residuals are $\Delta[\text{Fe}/\text{H}] = +0.029 \pm 0.121$ dex (MAD = 0.056 dex), demonstrating excellent agreement between our photometric-Bayesian metallicities and independent high-resolution spectroscopy. The mean offset of only +0.029 dex is well within the systematic uncertainty of isochrone-based metallicity determinations (≤ 0.1 dex) and is consistent with zero at the $\sim 0.2\sigma$ level. The tight MAD of 0.056 dex underscores the reliability of the Gaia XP photometric prior combined with the nested-sampling posterior in recovering [Fe/H] values that are close to spectroscopic ground truth.

The 127 OCCAM clusters in common span Galactocentric radii $R_{\text{GC}} = 6.0\text{--}16.3$ kpc (median 9.6 kpc), heliocentric distances of 88–6 888 pc (median 2 440 pc), and ages $\log(\text{Age}/\text{yr}) = 6.7\text{--}9.7$ (median 8.76); 70 per cent have $\log(\text{Age}/\text{yr}) \geq 8.5$, confirming that the subsample is dominated by intermediate-to-old disc clusters spanning a wide range of Galactocentric radii (J. Donor et al. 2020).

To assess the role of the *Gaia* XP metallicity prior in the spectroscopic agreement, we split the OCCAM validation sample into clusters with ($N = 82$) and without ($N = 45$) an informative XP prior. For the XP-prior subsample the residuals are $\Delta[\text{Fe}/\text{H}] = +0.030 \pm 0.083$ dex (MAD = 0.047 dex), while for the non-XP subsample they are $+0.028 \pm 0.170$ dex (MAD = 0.066 dex). Two findings emerge from this decomposition. First, the mean offset is nearly identical (+0.030 vs. +0.028 dex), confirming that neither group is systematically biased with respect to MWM. Second, the scatter is substantially smaller for XP-prior clusters (std 0.083 vs. 0.170 dex), consistent with the tighter posterior widths seen in Fig. 6. Critically, even the non-XP group has a scatter (MAD = 0.066 dex) that is well below the 0.65 dex typical posterior width for that group, confirming that the CMD likelihood does constrain the metallicity despite the broad prior — the posterior is not simply a copy of the prior, but the constraint is weaker and the reported uncertainty faithfully reflects this. Users of the catalogue who require tight individual metallicity estimates should preferentially select clusters with an informative XP prior (flaggable via the cross-match with the Gaia XP catalogue).

The small MAD = 0.056 dex across the full OCCAM sample — well within the systematic uncertainty of isochrone-based metallicity determinations ($\lesssim 0.1$ dex) — confirms that the photometric metallicity scale of our catalogue is consistent with independent high-resolution spectroscopy across the full range of ages, distances, and Galactic positions represented in the validation sample. The comparison is illustrated in Fig. 9 (one-to-one plot with summary statistics).

6. SUMMARY AND CONCLUSIONS

We have presented a homogeneous determination of fundamental astrophysical parameters — age, initial stellar metallicity (Z_{ini} , converted to [Fe/H]), heliocentric distance, and selective extinction $E(G_{\text{BP}} - G_{\text{RP}})$ — for 5 056 open clusters drawn from the Unified Cluster Catalogue (UCC; G. I. Perren et al. 2023). The analysis employs Bayesian Nested Sampling (J. S. Speagle 2020) coupled with PARSEC isochrones (A. Bressan et al. 2012; P. Marigo et al. 2017) in the Gaia DR3 photometric system (Gaia Collaboration et al. 2021), constituting the largest uniformly derived open-cluster parameter catalogue to date. The principal findings are summarised below.

1. *Pipeline and priors.* Each cluster is modelled in a four-dimensional parameter space [$\log(\text{Age}/\text{yr})$, Z_{ini} , d_{pc} , $E(G_{\text{BP}} - G_{\text{RP}})$]. Age priors are uniform over $\log(\text{Age}/\text{yr}) \in [6, 10]$ for all clusters. Distance priors are constructed as trun-

Comparison with Literature Catalogues

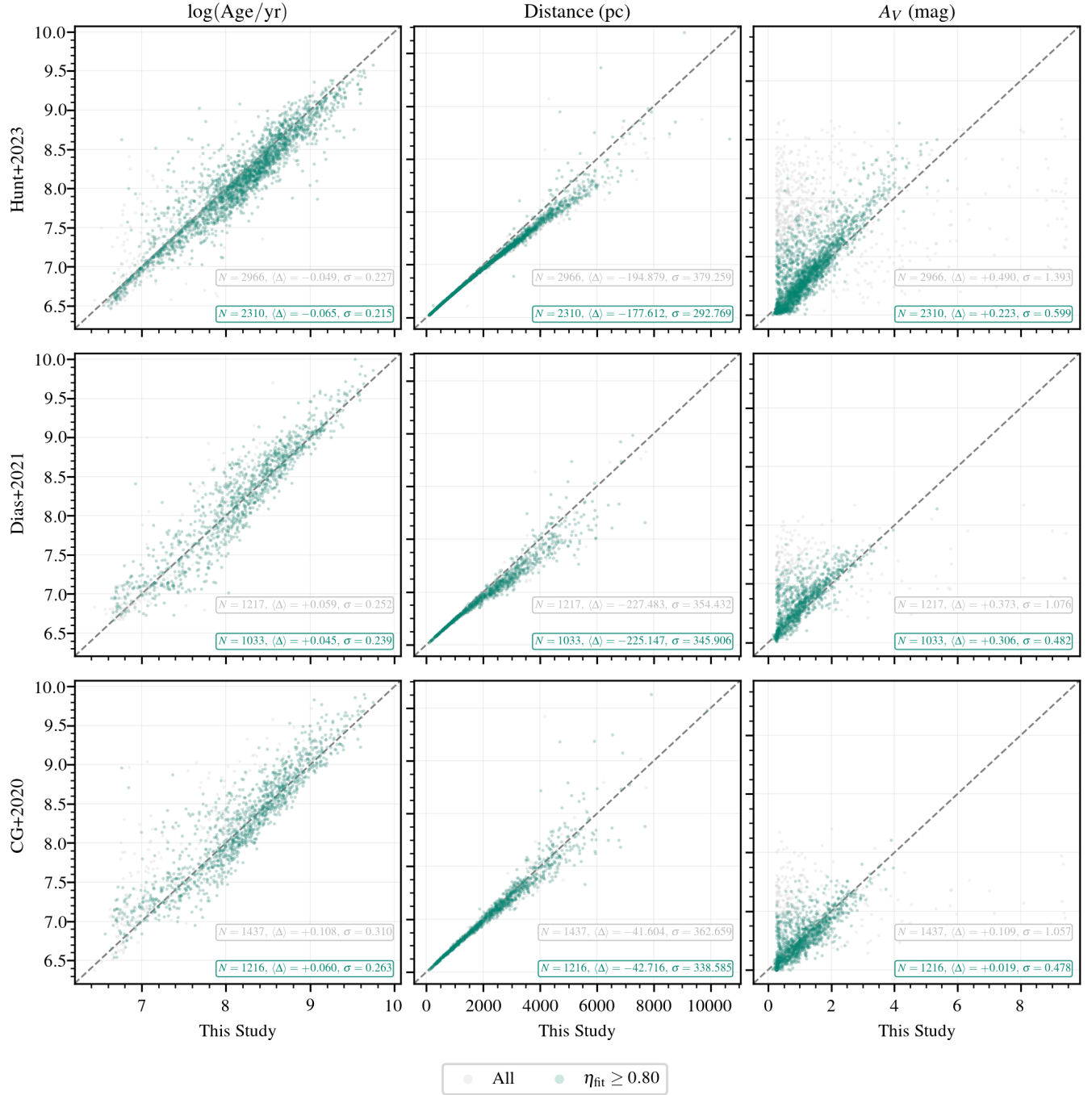


Figure 8. Scatter comparison of age ($\log(\text{Age}/\text{yr})$), distance, and A_G between this work and three photometric catalogues. Rows (top to bottom): Hunt et al. (2023), Dias et al. (2021), Cantat-Gaudin et al. (2020). Grey points show the full sample; teal points show clusters with $\eta_{\text{fit}} \geq 0.80$. Statistics (N , $\langle \Delta \rangle$, σ) for each panel are given in the lower right corner. Dashed lines indicate the 1:1 relation.

Table 1. Summary of parameter offsets between this work and four reference catalogues for the high-quality subset ($\eta_{\text{fit}} \geq 0.80$). Residuals are defined as $\Delta X = X_{\text{this work}} - X_{\text{ref}}$. $\langle \Delta \rangle$ is the mean offset, σ the standard deviation, and MAD the median absolute deviation from the median residual.

Reference	Parameter	N	$\langle \Delta \rangle$	σ	MAD
Hunt et al. (2023) ^a	$\Delta \log(\text{Age/yr})$ (dex)	2 310	+0.065	0.215	0.093
	Δd (pc)		+178	293	100
	ΔA_G (mag)		-0.223	0.599	0.252
Dias et al. (2021) ^b	$\Delta \log(\text{Age/yr})$ (dex)	1 033	-0.045	0.239	0.147
	Δd (pc)		+225	346	122
	$\Delta[\text{Fe}/\text{H}]$ (dex)		-0.029	0.151	0.082
Cantat-Gaudin et al. (2020) ^c	$\Delta \log(\text{Age/yr})$ (dex)	1 216	-0.060	0.263	0.144
	Δd (pc)		+43	339	55
	ΔA_G (mag)		-0.019	0.478	0.199
OCCAM DR19 (2024) ^d	$\Delta[\text{Fe}/\text{H}]$ (dex)	127	+0.029	0.121	0.056

^aE. L. Hunt & S. Reffert (2023).

^bW. S. Dias et al. (2021).

^cT. Cantat-Gaudin et al. (2020).

^dJ. M. Otto et al. (2026). OCCAM DR19 provides MWM spectroscopic $[\text{Fe}/\text{H}]$ and represents an independent spectroscopic validation of the photometric metallicity scale.

NOTE—All statistics computed for clusters with $\eta_{\text{fit}} \geq 0.80$ and valid values in both catalogues. A_G values for this work are computed from the posterior median $E(G_{\text{BP}} - G_{\text{RP}})$ using $A_G = K_{A_G/E(G_{\text{BP}} - G_{\text{RP}})} \times E(G_{\text{BP}} - G_{\text{RP}}) = 1.890 \times E(G_{\text{BP}} - G_{\text{RP}})$ (S. Wang & X. Chen 2019). Reference catalogue extinctions originally reported as A_V are converted to A_G via $A_G = A_V \times (K_{A_G/E(G_{\text{BP}} - G_{\text{RP}})} / K_{A_V/E(G_{\text{BP}} - G_{\text{RP}})}) = A_V \times 0.787$.

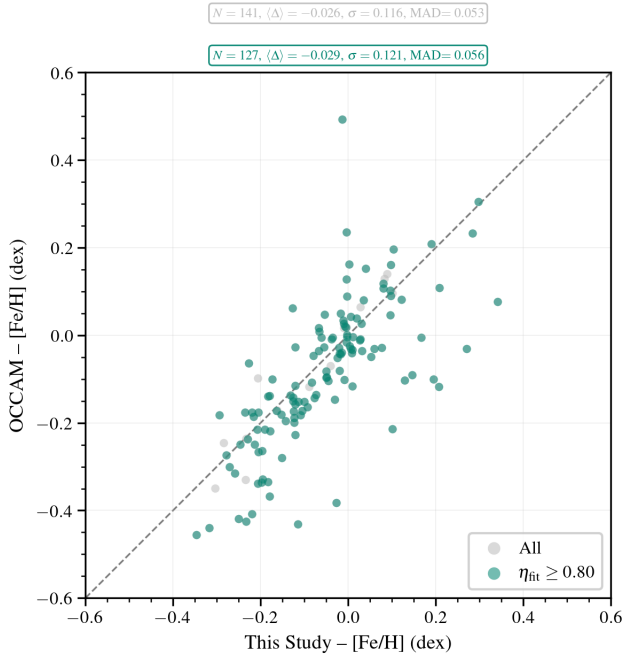


Figure 9. One-to-one comparison between photometric $[\text{Fe}/\text{H}]$ (this work) and MWM spectroscopic $[\text{Fe}/\text{H}]$ from the OCCAM DR19 catalogue (J. M. Otto et al. 2026) for the $\eta_{\text{fit}} \geq 0.80$ subset (teal) and the full sample (grey). The dashed line shows the 1:1 relation. Statistics (N , mean offset, σ , MAD) are shown in the panel.

ated Gaussians centred on the Gaia DR3 median parallax of cluster members. Metallicity priors are informed by Gaia XP spectrophotometric $[\text{Fe}/\text{H}]$ estimates for 1346 clusters with at least three member stars, serving as an informative starting point rather than a hard constraint; a broad uniform prior $[-0.5, +0.5]$ dex is adopted otherwise. Crucially, metallicity is treated as a fully free parameter throughout: the nested sampler explores the entire prior volume without imposing any assumed external abundance model, solar-neighbourhood metallicity, or other external chemical constraint. Extinction priors are anchored to SFD dust maps with a distance-dependent attenuation correction. All posterior inferences were performed on the TRUBA high-performance computing facility using DYNESTY’s multi-ellipsoidal sampler with $N_{\text{live}} = 400$ live points.

2. *Sample and quality.* Of the 5 056 processed clusters (2 121 AA-class and 2 767 AB-class), 3 766 (74.5 per cent) attain a high-quality fit flag $\eta_{\text{fit}} \geq 0.80$, indicating well-constrained posteriors and reliable convergence. The remaining clusters have broader posteriors, typically due to sparse member-

ship, unfavourable photometric depth, or strong differential reddening; such entries are retained in the catalogue with their η_{fit} flag, as broad posteriors reflect genuine photometric uncertainty rather than a failure of the inference and remain useful for statistical ensemble studies when appropriate quality thresholds are applied.

3. *Parameter distributions.* The derived ages span $\log(\text{Age}/\text{yr}) = 6.53\text{--}9.74$ with a median of 8.33 (MAD = 0.34 dex), consistent with a disc population dominated by intermediate-age clusters. Heliocentric distances range from 88 to 19 011 pc, with a median of 2 150 pc, extending the well-sampled Solar neighbourhood out to the outer disc. Photometric metallicities span $[\text{Fe}/\text{H}] = -1.17$ to $+0.42$ dex (median $+0.002$ dex, MAD = 0.064 dex), and total visual extinctions A_G reach up to 7.37 mag (median 1.07 mag).
4. *Validation against literature catalogues.* Comparison with E. L. Hunt & S. Reffert (2023) ($N = 2310$ clusters in common) yields $\Delta \log(\text{Age}) = +0.065 \pm 0.215$ (MAD = 0.093), a distance offset of $+178 \pm 293$ pc (MAD = 100 pc), and an extinction offset $\Delta A_V = -0.223 \pm 0.599$ mag (MAD = 0.252 mag), with no statistically significant systematic age bias. Comparison with W. S. Dias et al. (2021) ($N = 1\,033$) gives $\Delta \log(\text{Age}) = -0.045 \pm 0.239$ (MAD = 0.147), $\Delta d = +225 \pm 346$ pc (MAD = 122 pc), and $\Delta[\text{Fe}/\text{H}] = -0.029 \pm 0.151$ dex (MAD = 0.082 dex). Agreement with T. Cantat-Gaudin et al. (2020) ($N = 1\,216$) is similarly close: $\Delta \log(\text{Age}) = -0.060 \pm 0.263$ (MAD = 0.144) and $\Delta d = +43 \pm 339$ pc (MAD = 55 pc). Across all three photometric catalogues the systematic offsets in age remain below 0.07 dex in absolute value, demonstrating the robustness of the PARSEC-based inference.
5. *Spectroscopic metallicity validation.* Cross-matching with the OCCAM DR19 catalogue of spectroscopic open-cluster metallicities (J. M. Otto et al. 2026) ($N = 127$ clusters in common) yields $\Delta[\text{Fe}/\text{H}] = +0.029 \pm 0.121$ dex (MAD = 0.056 dex), confirming that the photometrically derived metallicities are consistent with independent high-resolution spectroscopic measurements to well within the systematic uncertainty of isochrone-based methods (≤ 0.1 dex). This agreement holds across a wide range of ages ($\log(\text{Age}/\text{yr}) = 6.7\text{--}9.7$) and Galactocentric radii ($R_{\text{GC}} = 6\text{--}16$ kpc), spanning the diversity of disc cluster environments represented in the present catalogue.

6. *Scientific applications.* The catalogue provides the largest homogeneous open-cluster parameter set to date derived with fully free photometric metallicity — 5 056 clusters processed with a single, uniform Bayesian pipeline on *Gaia* DR3 data. It constitutes a self-consistent reference baseline for a broad range of Galactic science: reconstruction of the age–metallicity and age–velocity–dispersion relations of the disc; chemical tagging and identification of co-natal stellar populations; mapping of the three-dimensional dust distribution; and calibration of stellar evolution models. The photometric [Fe/H] values are derived without assuming any external abundance model, so they provide model-independent metallicity estimates that are directly comparable with spectroscopic surveys and can serve as photometric priors for forthcoming high-multiplex spectroscopic programmes (4MOST, WEAVE). The combination of precise *Gaia* DR3 membership lists (G. I. Perren et al. 2023) with Bayesian parameter estimation ensures that cluster-to-field contamination is minimised, making this catalogue particularly suited for statistical ensemble studies.
7. *Future prospects.* The arrival of *Gaia* DR4, with its improved astrometric solutions, extended photometric calibrations, and radial-velocity measure-

ments for a substantially larger fraction of cluster members, will enable further refinement of membership probabilities and tighter parallax-based distance priors. Incorporation of ground-based and space-based spectroscopic surveys (e.g. 4MOST, WEAVE) will allow spectroscopic metallicity priors to be applied to a much larger fraction of the sample, breaking the photometric age–metallicity degeneracy for metal-poor and heavily reddened clusters. Extension of the pipeline to the remaining UCC clusters of lower astrometric quality, as well as to embedded and very young clusters currently excluded by the membership quality cuts, represents a natural next step.

The parameter catalogue is publicly available through CDS/VizieR. The complete set of DYNASTY posterior samples (HDF5 format, one file per cluster) is archived on Zenodo, enabling full independent reproduction of all results and supporting user-defined re-analyses of individual cluster posteriors. The pipeline source code will be released on GitHub with a citable DOI; it is available on request until then. The tabulated posterior medians and credible intervals are designed to be directly usable for disc structure and chemical-evolution studies, while the published η_{fit} flags allow users to tailor quality cuts to the specific requirements of their analysis.

APPENDIX

A. CATALOGUE COLUMN DESCRIPTIONS

Table 2 lists all columns of the published open cluster parameter catalogue together with their units and descriptions. The catalogue contains 5 056 entries, one per cluster, and is made available in full through the CDS/VizieR service and as a supplementary machine-readable file accompanying this article. Each row provides posterior medians and asymmetric 1σ credible intervals (16th and 84th percentiles) for the four fitted parameters ($\log \text{Age}$, [Fe/H], d , $E(G_{\text{BP}} - G_{\text{RP}})$) together with the derived G -band extinction A_G , the fit-quality indicator η_{fit} , the nested-sampling convergence flag, and the log-evidence $\ln Z$. A representative sample of ten entries is reproduced in Table 3 to illustrate the format and typical parameter values.

Table 2. Description of the published catalogue columns. The full table of 5 056 clusters is available at CDS/VizieR; the posterior HDF5 chains are archived on Zenodo. All uncertainties are the 16th–50th and 50th–84th percentile intervals of the marginal posterior distributions.

Column	Unit	Description
Cluster	—	Cluster identifier (semicolon-separated aliases; primary name is the first token)
source	—	Pipeline source: AA, AB (UCC quality class)
N_members_mask	—	Number of member stars with membership probability $p \geq 0.75$ (used in the fit)
N_members_total	—	Total number of member stars in the UCC membership file
logAge_Med	dex	Posterior median of $\log(\text{Age}/\text{yr})$
logAge_ErrLo	dex	Lower 1σ uncertainty: median – 16th percentile
logAge_ErrHi	dex	Upper 1σ uncertainty: 84th percentile – median
Age_Med_Gyr	Gyr	Posterior median age in gigayears
Age_ErrLo_Gyr	Gyr	Lower age uncertainty (Gyr)
Age_ErrHi_Gyr	Gyr	Upper age uncertainty (Gyr)
FeH_Med	dex	Posterior median of $[\text{Fe}/\text{H}]$ (photometric)
FeH_Lo	dex	Lower 1σ uncertainty of $[\text{Fe}/\text{H}]$
FeH_Hi	dex	Upper 1σ uncertainty of $[\text{Fe}/\text{H}]$
Z_Med	—	Posterior median of initial metallicity Z_{ini}
Z_Lo	—	Lower 1σ uncertainty of Z_{ini}
Z_Hi	—	Upper 1σ uncertainty of Z_{ini}
Dist_Med_pc	pc	Posterior median heliocentric distance
Dist_Lo_pc	pc	Lower 1σ distance uncertainty
Dist_Hi_pc	pc	Upper 1σ distance uncertainty
E_BPRP_Med	mag	Posterior median colour excess $E(G_{\text{BP}} - G_{\text{RP}})$
E_BPRP_Lo	mag	Lower 1σ uncertainty of $E(G_{\text{BP}} - G_{\text{RP}})$
E_BPRP_Hi	mag	Upper 1σ uncertainty of $E(G_{\text{BP}} - G_{\text{RP}})$
eta_fit	—	Fit quality indicator η_{fit} (fraction of CMD members consistent with the best-fit isochrone; see §3.5)
Converged	—	Nested-sampling convergence flag ($\Delta \ln Z < 0.01$)
LogZ	—	Nested-sampling log-evidence $\ln Z$
LogZ_err	—	Uncertainty of $\ln Z$
A_G_Med	mag	Posterior median G -band extinction $A_G = 1.890 \times E(G_{\text{BP}} - G_{\text{RP}})$ (S. Wang & X. Chen 2019)
A_G_ErrLo	mag	Lower 1σ uncertainty of A_G
A_G_ErrHi	mag	Upper 1σ uncertainty of A_G

NOTE—The $[\text{Fe}/\text{H}]$ column is a photometric metallicity derived from the Bayesian nested-sampling fit to the *Gaia* DR3 CMD. Clusters with an informative *Gaia* XP spectrophotometric metallicity prior ($n_{\text{XP}} \geq 3$ member stars; $N = 1\,346$ in the full catalogue, $N = 755$ in the high-quality subset) have significantly narrower $[\text{Fe}/\text{H}]$ posteriors (median $\Delta[\text{Fe}/\text{H}] = 0.42$ dex) than clusters fitted with the broad uniform prior (median 0.65 dex; see Fig. 6). Users requiring tight individual metallicity estimates should preferentially use clusters with an informative XP prior. A_G is derived from the posterior $E(G_{\text{BP}} - G_{\text{RP}})$ using the extinction coefficient $K_{A_G/E(G_{\text{BP}} - G_{\text{RP}})} = 1.890$ (S. Wang & X. Chen 2019).

Table 3. First ten entries of the open cluster parameter catalogue (Table 2 describes all columns). Uncertainties are the 16th–84th percentile credible intervals of the posterior distribution. The complete table of 5 056 clusters is available in machine-readable form at CDS/VizieR and as a supplementary file with this article.

Cluster	Source	N_*	$\log(\text{Age}/\text{yr})$	$[\text{Fe}/\text{H}]$ (dex)	d (pc)	$E(G_{\text{BP}} - G_{\text{RP}})$ (mag)	A_G (mag)	η_{ft}
ASCC10	AA	80	$7.999^{+0.373}_{-0.346}$	$+0.049^{+0.289}_{-0.346}$	662^{+15}_{-15}	$0.283^{+0.148}_{-0.165}$	0.534	0.988
ASCC100	AA	85	$7.824^{+0.348}_{-0.346}$	$-0.015^{+0.340}_{-0.329}$	357^{+15}_{-15}	$0.134^{+0.151}_{-0.094}$	0.254	0.918
ASCC101	AA	167	$8.322^{+0.336}_{-0.346}$	$-0.024^{+0.331}_{-0.319}$	398^{+15}_{-15}	$0.139^{+0.143}_{-0.094}$	0.263	0.970
ASCC103	AA	253	$8.153^{+0.356}_{-0.349}$	$-0.003^{+0.325}_{-0.337}$	498^{+15}_{-15}	$0.141^{+0.143}_{-0.096}$	0.266	0.964
ASCC105	AA	115	$7.926^{+0.360}_{-0.349}$	$+0.039^{+0.304}_{-0.365}$	561^{+15}_{-15}	$0.174^{+0.143}_{-0.116}$	0.330	0.965
ASCC11	AA	306	$8.480^{+0.374}_{-0.375}$	$+0.040^{+0.318}_{-0.349}$	855^{+15}_{-15}	$0.276^{+0.166}_{-0.156}$	0.522	0.990
ASCC111	AA	60	$7.996^{+0.373}_{-0.370}$	$+0.090^{+0.273}_{-0.381}$	855^{+15}_{-15}	$0.232^{+0.156}_{-0.144}$	0.439	1.000
ASCC112	AA	231	$8.309^{+0.354}_{-0.348}$	$-0.011^{+0.318}_{-0.327}$	651^{+15}_{-15}	$0.172^{+0.150}_{-0.113}$	0.326	0.952
ASCC113	AA	352	$8.322^{+0.341}_{-0.346}$	$-0.014^{+0.298}_{-0.321}$	567^{+15}_{-15}	$0.162^{+0.142}_{-0.106}$	0.307	0.994
ASCC114	AA	165	$7.545^{+0.366}_{-0.358}$	$+0.021^{+0.327}_{-0.353}$	936^{+15}_{-15}	$0.158^{+0.169}_{-0.110}$	0.299	0.976

NOTE—This table is published in its entirety in machine-readable form as a supplementary file. A portion is shown here for guidance regarding its form and content.

ACKNOWLEDGMENTS

This work was supported by the Scientific and Technological Research Council of Turkey (TÜBİTAK) under grant 125F465. The numerical calculations reported in this paper were fully performed at TUBITAK ULAKBIM, High Performance and Grid Computing Center (TRUBA resources). This work has made use of data from the European Space Agency (ESA) mission *Gaia* (<https://www.cosmos.esa.int/gaia>), processed by the *Gaia* Data Processing and Analysis Consortium (DPAC, <https://www.cosmos.esa.int/web/gaia/dpac/consortium>). This research has made use of the ASTROPY package (Astropy Collaboration et al. 2013) and DYNESTY (J. S. Speagle 2020).

DATA AVAILABILITY

The full parameter catalogue — including posterior medians, 16th/84th percentile credible intervals, the fit-

quality indicator η_{fit} , convergence flag, and log-evidence $\ln Z$ for all 5 056 clusters — is available through the CDS/VizieR service (<https://cdsarc.cds.unistra.fr>).

The complete set of DYNESTY posterior samples in HDF5 format (one file per cluster, totalling $\sim 5\,000$ files) is archived separately on Zenodo (<https://doi.org/10.5281/zenodo.XXXXXXX>). These files contain the full nested-sampling chains and can be used to reproduce all figures and statistics in this paper, or to carry out independent analyses of individual cluster posteriors without re-running the pipeline.

The pipeline source code is being prepared for public release on GitHub (<https://github.com/oplevne/uccns-parsec>); it will be assigned a citable DOI via Zenodo upon release. In the interim, the code is available upon reasonable request to the corresponding author (olcayplevne@istanbul.edu.tr).

REFERENCES

- Andrae, R., Rix, H.-W., & Chandra, V. 2023, *A&AS*, 267, 8, doi: [10.3847/1538-4365/acd53e](https://doi.org/10.3847/1538-4365/acd53e)
- Astropy Collaboration, Robitaille, T. P., Tollerud, E. J., et al. 2013, *A&A*, 558, A33, doi: [10.1051/0004-6361/201322068](https://doi.org/10.1051/0004-6361/201322068)
- Bailer-Jones, C. A. L., Rybizki, J., Fouesneau, M., Demleitner, M., & Andrae, R. 2021, *AJ*, 161, 147, doi: [10.3847/1538-3881/abd806](https://doi.org/10.3847/1538-3881/abd806)
- Bressan, A., Marigo, P., Girardi, L., et al. 2012, *MNRAS*, 427, 127, doi: [10.1111/j.1365-2966.2012.21948.x](https://doi.org/10.1111/j.1365-2966.2012.21948.x)
- Campello, R. J. G. B., Moulavi, D., & Sander, J. 2013, *Advances in Knowledge Discovery and Data Mining*, 160
- Cantat-Gaudin, T. 2022, *Universe*, 8, 111, doi: [10.3390/universe8020111](https://doi.org/10.3390/universe8020111)
- Cantat-Gaudin, T., Anders, F., Castro-Ginard, A., et al. 2020, *A&A*, 640, A1, doi: [10.1051/0004-6361/202038192](https://doi.org/10.1051/0004-6361/202038192)
- Casamiquela, L., Tarricq, Y., Soubiran, C., et al. 2021, *A&A*, 652, A25, doi: [10.1051/0004-6361/202039951](https://doi.org/10.1051/0004-6361/202039951)
- Chen, Y., Girardi, L., Bressan, A., et al. 2014, *MNRAS*, 444, 2525, doi: [10.1093/mnras/stu1605](https://doi.org/10.1093/mnras/stu1605)
- De Angeli, F., Weiler, M., Montegriffo, P., et al. 2023, *A&A*, 674, A2, doi: [10.1051/0004-6361/202243680](https://doi.org/10.1051/0004-6361/202243680)
- Dias, W. S., Alessi, B. S., Moitinho, A., & Lépine, J. R. D. 2002, *A&A*, 389, 871, doi: [10.1051/0004-6361:20020668](https://doi.org/10.1051/0004-6361:20020668)
- Dias, W. S., Monteiro, H., Moitinho, A., et al. 2021, *MNRAS*, 504, 356, doi: [10.1093/mnras/stab770](https://doi.org/10.1093/mnras/stab770)
- Donor, J., Frinchaboy, P. M., Cunha, K., et al. 2020, *AJ*, 159, 199, doi: [10.3847/1538-3881/ab77bc](https://doi.org/10.3847/1538-3881/ab77bc)
- Drimmel, R., & Spergel, D. N. 2001, *ApJ*, 556, 181, doi: [10.1086/321611](https://doi.org/10.1086/321611)
- Gaia Collaboration, Brown, A. G. A., Vallenari, A., et al. 2018, *A&A*, 616, A1, doi: [10.1051/0004-6361/201833051](https://doi.org/10.1051/0004-6361/201833051)
- Gaia Collaboration, Brown, A. G. A., Vallenari, A., et al. 2021, *A&A*, 649, A1, doi: [10.1051/0004-6361/202039657](https://doi.org/10.1051/0004-6361/202039657)
- Gaia Collaboration, Vallenari, A., Brown, A. G. A., et al. 2023, *A&A*, 674, A1, doi: [10.1051/0004-6361/202243940](https://doi.org/10.1051/0004-6361/202243940)
- Hunt, E. L., & Reffert, S. 2021, *A&A*, 646, A104, doi: [10.1051/0004-6361/202039341](https://doi.org/10.1051/0004-6361/202039341)
- Hunt, E. L., & Reffert, S. 2023, *A&A*, 673, A114, doi: [10.1051/0004-6361/202346267](https://doi.org/10.1051/0004-6361/202346267)
- Hunt, E. L., & Reffert, S. 2024, *A&A*, 686, A42, doi: [10.1051/0004-6361/202348929](https://doi.org/10.1051/0004-6361/202348929)
- Kharchenko, N. V., Piskunov, A. E., Röser, S., Schilbach, E., & Scholz, R.-D. 2013, *A&A*, 558, A53, doi: [10.1051/0004-6361/201322302](https://doi.org/10.1051/0004-6361/201322302)
- Lindgren, L., Klioner, S. A., Hernández, J., et al. 2021, *A&A*, 649, A2, doi: [10.1051/0004-6361/202039653](https://doi.org/10.1051/0004-6361/202039653)
- Lindgren, L., et al. 2018, *A&A*, 616, A2, doi: [10.1051/0004-6361/201832727](https://doi.org/10.1051/0004-6361/201832727)
- Marigo, P., Girardi, L., Bressan, A., et al. 2017, *ApJ*, 835, 77, doi: [10.3847/1538-4357/835/1/77](https://doi.org/10.3847/1538-4357/835/1/77)
- McInnes, L., & Healy, J. 2017, arXiv e-prints, arXiv:1705.07321, doi: [10.48550/arXiv.1705.07321](https://doi.org/10.48550/arXiv.1705.07321)
- Mészáros, S., Jofré, P., Johnson, J. A., et al. 2025, *AJ*, 170, 96, doi: [10.3847/1538-3881/ade4b9](https://doi.org/10.3847/1538-3881/ade4b9)
- Otto, J. M., Frinchaboy, P. M., Myers, N. R., et al. 2026, *AJ*, 171, 91, doi: [10.3847/1538-3881/ae28d8](https://doi.org/10.3847/1538-3881/ae28d8)

- Perren, G. I., Vázquez, R. A., Piatti, A. E., et al. 2023, MNRAS, 526, 4107, doi: [10.1093/mnras/stad2826](https://doi.org/10.1093/mnras/stad2826)
- Schlafly, E. F., & Finkbeiner, D. P. 2011, ApJ, 737, 103, doi: [10.1088/0004-637X/737/2/103](https://doi.org/10.1088/0004-637X/737/2/103)
- Schlegel, D. J., Finkbeiner, D. P., & Davis, M. 1998, ApJ, 500, 525, doi: [10.1086/305772](https://doi.org/10.1086/305772)
- Skilling, J. 2004, in American Institute of Physics Conference Series, Vol. 735, Bayesian Inference and Maximum Entropy Methods in Science and Engineering, ed. R. Fischer, R. Preuss, & U. V. Toussaint, 395–405, doi: [10.1063/1.1835238](https://doi.org/10.1063/1.1835238)
- Speagle, J. S. 2020, MNRAS, 493, 3132, doi: [10.1093/mnras/staa278](https://doi.org/10.1093/mnras/staa278)
- Tarricq, Y., Soubiran, C., Casamiquela, L., et al. 2021, A&A, 647, A19, doi: [10.1051/0004-6361/202039388](https://doi.org/10.1051/0004-6361/202039388)
- Wang, S., & Chen, X. 2019, ApJ, 877, 116, doi: [10.3847/1538-4357/ab1c61](https://doi.org/10.3847/1538-4357/ab1c61)